Supporting Information

Hot Electrons Do the Impossible: Plasmon-Induced Dissociation of H_2 on Au

Shaunak Mukherjee,[†,#] Florian Libisch,*[‡,#] Nicolas Large,[§,#] Oara Neumann,[†,#] Lisa V. Brown,[†,‡,§,#] Jin Cheng,*[§,#] J. Britt Lassiter,[‡,§,#] Emily A. Carter,*[†,‡,§,#] Peter Nordlander,[§,#] and Naomi J. Halas[†,‡,§,#]

[†]Department of Chemistry, [‡]Department of Electrical and Computer Engineering, [§]Department of Physics and Astronomy, and [#]Laboratory for Nanophotonics, Rice University, 6100 Main Street, Houston, Texas 77005, USA

*Department of Mechanical and Aerospace Engineering, Program in Applied and Computational Mathematics, and the Andlinger Center for Energy and the Environment, Princeton University,

Princeton, New Jersey 08544, USA

Contents

Materials and Methods used

S1. Au/TiO_2 photocatalyst sample preparation

The Au/TiO_2 photocatalyst samples were prepared by deposition-precipitation method[1-3] using 1(M) NaOH as the basification agent. Briefly, commercially available Degussa P25-TiO_2 nanopowder (Sigma-Aldrich 718467-100G, average surface area 35-65 m^2/g, average particle diameter 20-30 nm) was dried and activated in an oven at 373 K for at least 24 hours prior to use. Different AuNP wt% supported over TiO_2 is obtained by stirring 100 mL solution containing different concentrations of $HAuCl_4.3H_2O$ (for example, 0.082 g, 0.165 g, 0.335 g, 0.667 g, 1.32 g $HAuCl_4,3H_2O$ (Sigma-Aldrich,520918-5G) added for 0.57%, 1%, 1.75%, 2.25% and 3.23% Au loading) and 1 g of TiO_2 kept at 80^oC in the dark. The pH of the solution was adjusted using 1(M) NaOH. After 2 hours the photocatalysts were cooled and exhaustively washed with water by centrifuging at 3,800 rpm several times until the solution is free from Cl^- ions ($AgNO_3$ solution was used to test for Cl^- ions). The purified catalyst solution was kept overnight at 100^oC in an oven for drying and the next day the dried samples were crushed into powder in a porcelain boat and kept inside the oven at 300^oC for 2:30 hours. Subsequently the photocatalysts samples were cooled in absence of moisture and almost immediately loaded into the reaction chamber for experiment. These photocatalysts samples were found to be stable and reactive even after three months if they are kept in the dark inside desiccator to avoid photo decomposition and degradation by moisture.

S2. Characterization of structure and morphology JEOL 2100 Field Emission Gun Transmission Electron Microscope (JEM 2100F TEM) was used to acquire high resolution TEM images of the catalyst samples.

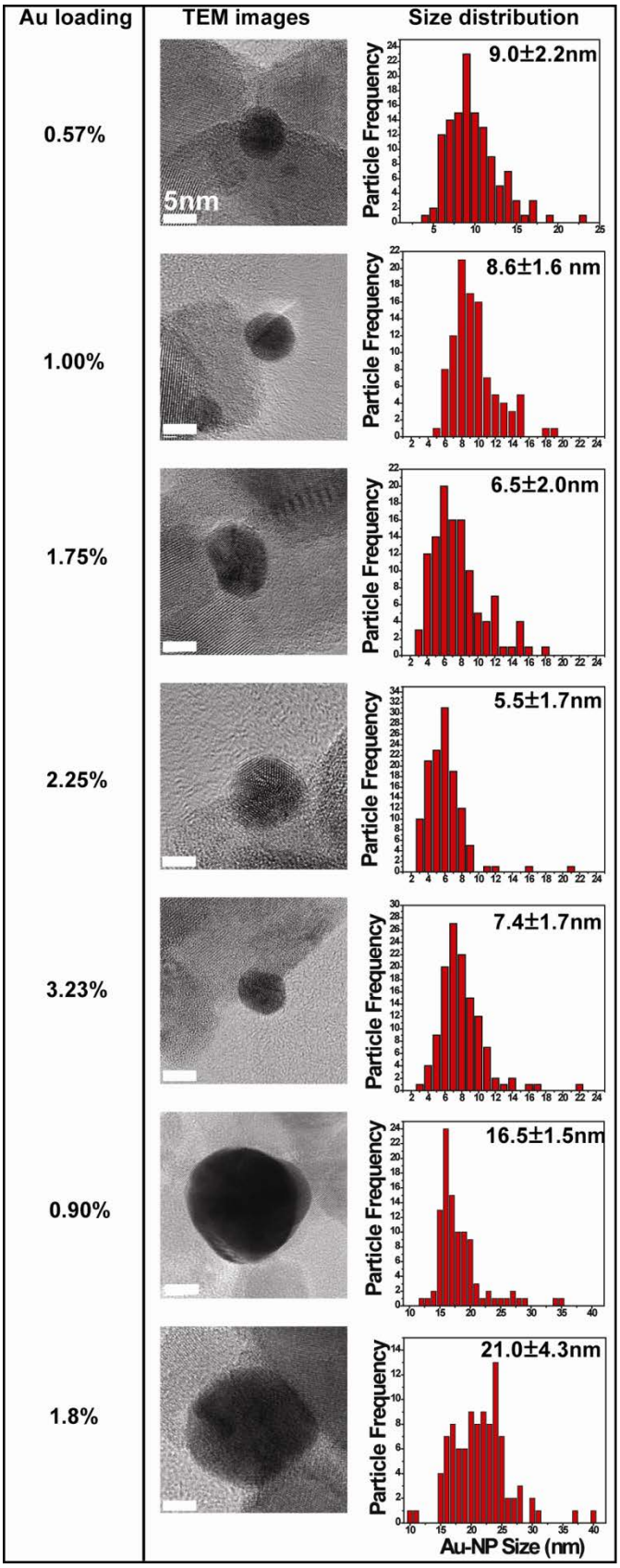
Au loading
TEM images
Size distribution
0.57%
5nm
9.0±2.2nm
1.00%
8.6±1.6 nm
1.75%
6.5±2.0nm
2.25%
5.5±1.7nm
3.23%
7.4±1.7nm
0.90%
16.5±1.5nm
1.8%
21.0±4.3nm
Particle Frequency
Au-NP Size (nm)

Figure S1 |TEM images and Size distribution High resolution TEM images and the corresponding size distribution of the Au/TiO_2 catalyst particles having different wt% of Au loading. The scale bar is 5 nm in each case. The mean size of Au NPs is based on counting the diameter of about 125 individual AuNP on each sample from their TEM images.

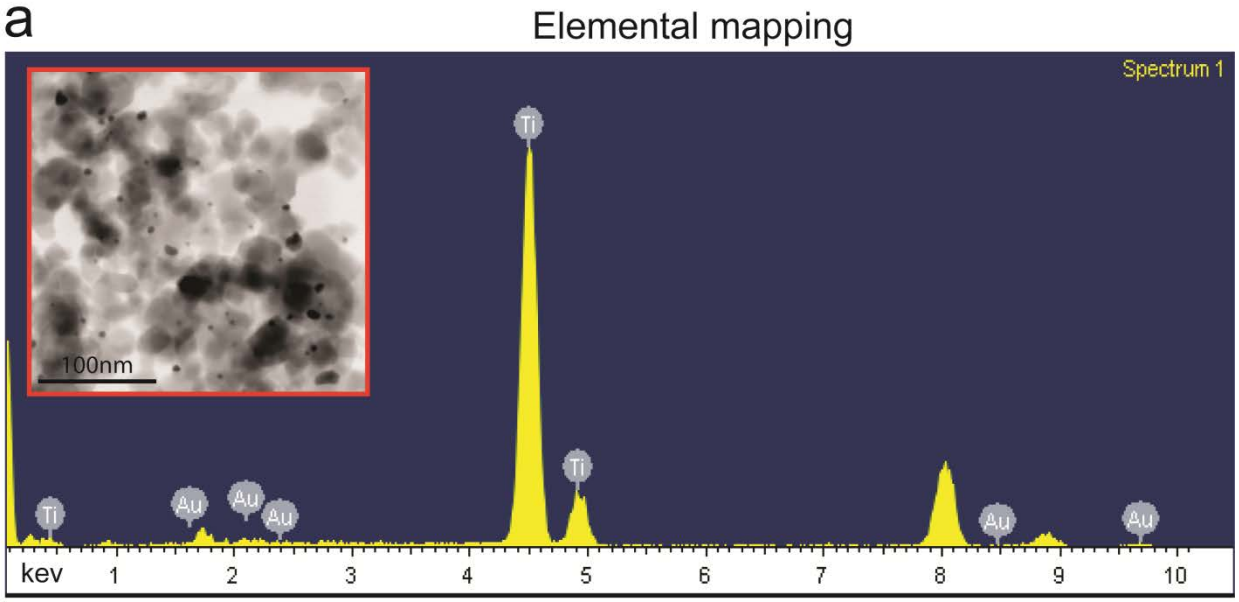

Figure S2| Energy dispersive X-ray Analysis of Au/TiO2 sample having 1.75% Au loading. a, EDS analysis of the area shown in the inset showing Au and Ti peaks. (Elemental peak positioned near 1, 8 and 9 keV originates from Cu TEM grids.)

S3. XPS characterization Au/TiO_2 samples were characterized using X-ray photoelectron spectroscopy (XPS) using PHI Quantera XPS. In each sample XPS was done at 4 different areas on the sample for consistent measurements. Binding energies of Au 4f as well as Ti (2p) peaks were measured. The Au wt% on each sample was represented by calculating Au $4f_{7/2}$ and Ti 2p (not shown in figure) peak area ratios. The XPS data of binding energy of Au is depicted in Fig.S2a and S2b. It is noted that in spite of increasing the Au content as well as increasing the size of the NP, the peak position of the $Au4f_{7/2}$ does not shift appreciably in successive samples (82.5 - 82.7 eV) which shows the similar electronic state of Au nanoparticles in different catalyst samples. The electronic state of the AuNP remain independent of the percentage of Au loading

or AuNP size, which was achieved using exactly constant synthetic condition for making these photocatalysts[4].The shift of the $4f_{7/2}$ binding energy from the ideal position of 83.9 eV representing Au^0 is due to sintering of the Au/TiO_2 catalysts as well as due to the fact that Au binds strongly with the oxygen vacancies of TiO_2, resulting in charge transfer between the Au and TiO_2[5, 6].

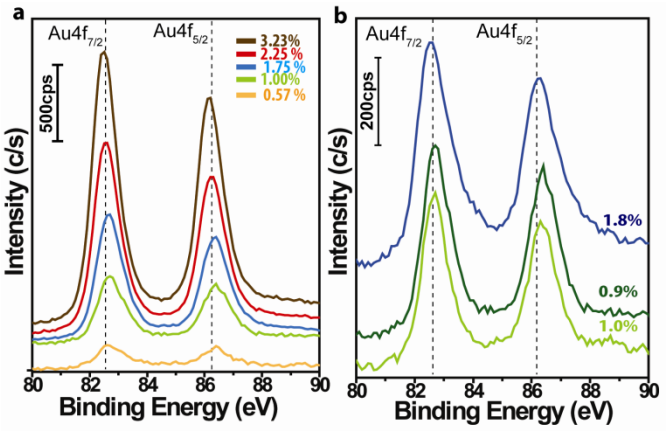

Figure S3 |Binding energy of Au 4f peaks of all Au/TiO_2 catalyst samples. (a) The Au 4f peaks of Au/TiO_2 samples tested for rate measurement studies as a function of increasing Au loading. (b) The Au 4f peaks of Au/TiO_2 samples tested for Au NP size dependence studies.

Table S3. Data obtained from XPS measurements.

Sample identity	*Ti (2p) ± SD**	*Au (4f) ± SD**
1	99.4 ± 0.09	0.57 ± 0.05
2	99.0 ± 0.13	1.00± 0.13
3	98.2 ± 0.22	1.75 ± 0.07
4	97.7 ± 0.17	2.25 ± 0.17

5	96.7 ± 0.25	3.23 ± 0.25
6	99.1 ± 0.07	0.90± 0.07
7	98.2± NA	1.8± NA

* Standard Deviation (SD) calculated over the data obtained from at least four different positions on the sample for verifying homogeneity of the analyzed sample.

(NA - not available)

S4.UV-Vis characterization The optical spectra of all powdered samples were measured using the Cary 5000 UV-Vis spectrometer equipped with Harrick Scientific Praying Mantis Diffuse Reflectance accessory for analysis of the powdered samples.

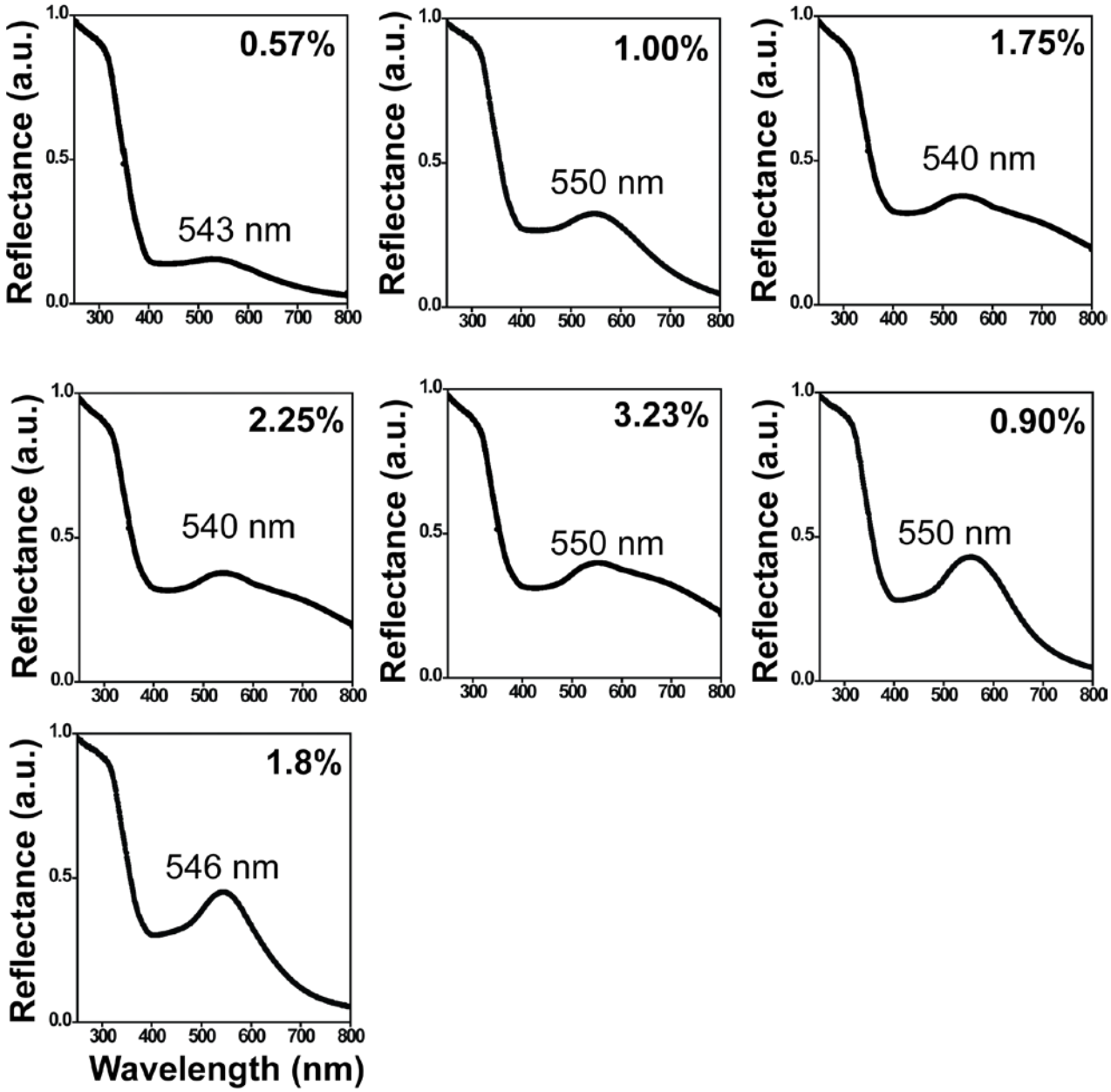

Figure S4 | Normalized Diffuse reflectance UV-Vis spectra of all powdered Au/TiO_2 samples with different wt% of Au loading (inset). Each spectrum shows the dipolar plasmon resonance located around 540-550 nm indicated in each spectrum panel and a steep feature starting from 400 nm due to TiO_2 bandgap. Due to small sizes of Au NPs as compared to the wavelength of light used much less tunability or shift of surface plasmon peak was observed in different samples. The inhomogeneous broadening and damped plasmon is also a direct consequence of the size distribution of the small Au NPs[7, 8].

S5 Experimental setup

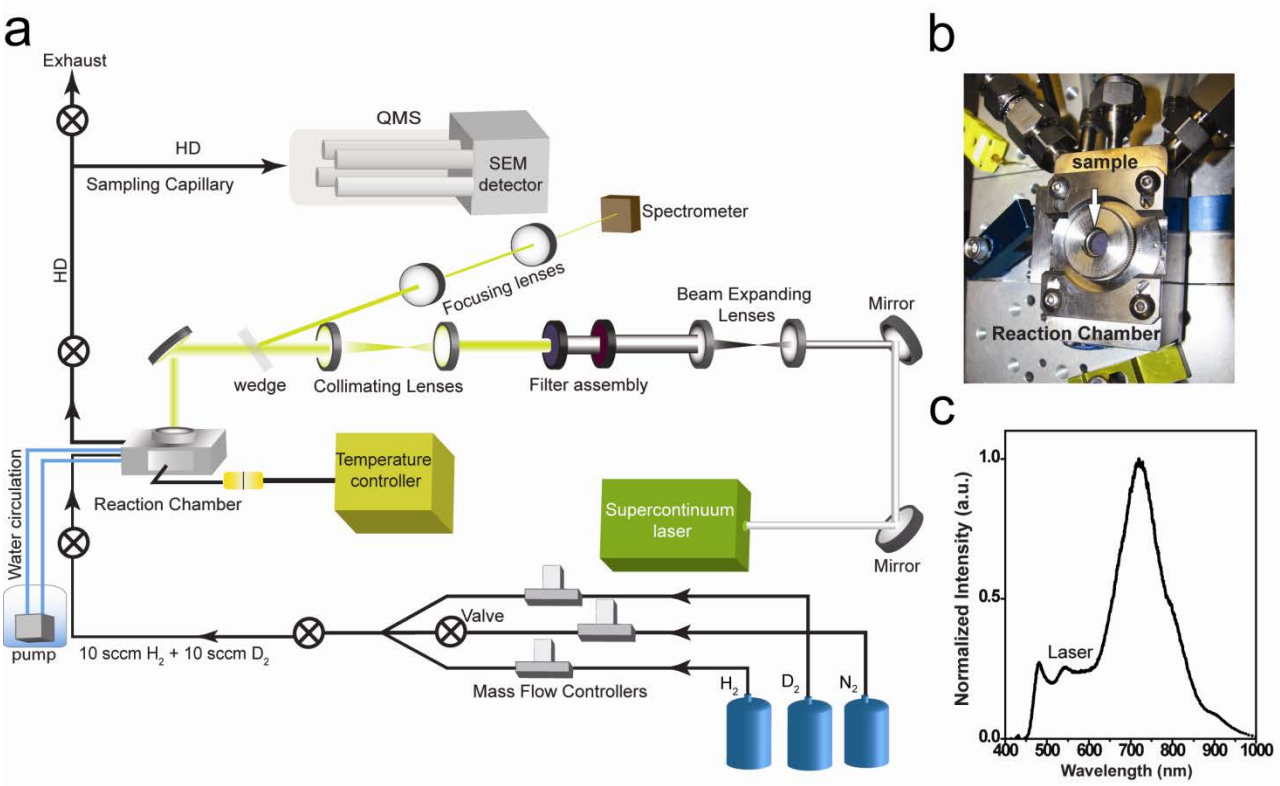

Figure S5 |Experimental Setup a, The overall experimental setup. **b,** Image of the stainless steel micro-reactor system used for dissociation reaction. The purple color of the Au/TiO_2 powdered sample loaded inside the sample cup is visible through the quartz window. **c,** Intensity spectrum of the supercontinuum laser as a function of wavelength.

S5 Measurement procedures: For photocatalytic rate measurements, Harrick Scientific stainless steel 316 reaction chamber (HVC-MRA-4) is used which is equipped with ~ $1cm^2$ quartz glass window. The photocatalytic powdered sample is loaded into a sample cup holder which is about 8 mm in diameter and about 4 mm in depth. The K type thermocouple and heating module is attached to this cup. The output temperature profile is read using a temperature controller ATC-024-3 (Harrick Scientific) to accurately monitor and control the temperature within 1^oC resolution. The temperature controller and the thermocouple were calibrated up to 750^oC for each degree centigrade change in temperature. In addition before starting experiment with a new photocatalyst sample it is re-calibrated. Water is circulated around the chamber to

keep the catalysts system at a defined temperature very precisely. The thermocouple senses the temperature change of the sample cup holder which in turn gives the temperature of the powdered sample kept in the cup. The chamber was purged with research purity N_2 for 3-5 days each time before loading any sample to clean the chamber of moisture and any other gases. Au/TiO_2 photocatalyst powdered sample was tightly loaded into the reaction chamber and again 20 sccm N_2 for flowed into the chamber at room temperature for a whole day. After that 10 sccm of H_2 (Matheson, UHP 99.9999% research grade) and 10 sccm of D_2 (Matheson, UHP 99.999% research grade) were flowed into the chamber at room temperature. Gas flow was controlled using programmable mass flow controller systems (Sierra instruments, Smart trak 100). Flowing H_2 and D_2 for at least 10-12 hrs over the catalyst is crucial to obtain a stable baseline. After this, rate measurements were carried out using the quadrupole mass spectrometer (QMS) fitted to the outlet of this chamber for monitoring products. All QMS measurements were performed using Hiden HPR-20 QIC Bench-top Gas Analysis System which includes High resolution Hiden HAL 1051-9 RC system with mass range 0 to 50 amu and with dual Faraday/single channel electron multiplier detector operating at an base pressure of $2.2 – 2.3x10^{-6}$ Torr. Before starting the actual measurement with the mass spectrometer, at first the HD baseline was monitored for 3hrs until we get a stable flat baseline. At room temperature while monitoring the rate of HD, the system was allowed to reach steady state for 5-10 minutes in the dark conditions following which the supercontinuum laser (Fianium) having different intensities was incident on the sample through the quartz window for 5-10 minutes whereby there is almost instant increase in the observed rate of HD. After that the laser is switched off and the reactor is kept in dark condition when the rate of HD formation reverts back to the initial value. The net photocatalytic rate was obtained by

subtracting the rate of HD while laser was off (auto dissociation rate) to the rate while the laser was on (actual photodissociation rate) to get rid of baseline.

For higher temperature photothermal rate measurements, the chamber was water cooled to keep the temperature constant and the catalyst was allowed to reach steady state for a longer time (20-40 mins) in the dark until the steady state is reached. The key for accuracy in temperature readout is to keep the sample reach steady state at any temperature. This ensures that local temperature of the particles in dark conditions is not different than the temperature measured using the sample cup sensor. The steady state is confirmed by the steady flat baseline of HD formation measured real time using the quadrupole mass spectroscopy. In addition after the photocatalyst sample has reached steady state at each final temperature, IR temperature sensor (Omega Engineering) is used to confirm the final temperature.

Intensity dependence measurements were carried out at both room temperature and a constant temperature of 373 K while the laser intensity was varied using a set of neutral density filters. Four different photocatalyst with different Au loading (0.57, 1.75, 2.25 and 3.23 %) was used in this experiment. The laser power was varied at an increment of 50 mW starting from 100 mW to 1 W (except for the sample with 0.57 % Au loading where 100 mW increment was used due to low reactivity). A CMOS sensor (Thorlabs DCC1545M) was used to measure the spot size (7 mm) of the laser. Power of the laser was measured using a thermal power sensor (Thorlabs S314C and PM100 USB). A 450 nm long pass filter was used in the beam path of the laser to ensure it does not excite the bandgap of TiO_2. The laser spectrum was recorded using ocean optics spectrometer connected to the setup.

For wavelength dependent rate measurements different band pass filters (Thorlabs FKB-VIS-40) were used. These filters have a 40 nm bandwidth and they are ~50 nm apart in wavelengths. A set of focusing telescope lenses were used to increase or decrease the spot size of the laser before it can damage delicate optics in the setup specially the filters (Fig. S5). The transmitted laser

after the filters was operated at 50 mW laser power. This was performed using a set of neutral density filters before rate measurement for each particular filter. With addition of filter each time on/off of laser light was performed and rate was measured as usual.

S6. Effect of plasmonic heating To elucidate plasmonic heating effect due to AuNPs, we assume that AuNPs are well separated to be acting as individual nanoparticles so that any influence due to plasmonic coupling can be disregarded. This is a fair assumption as the concentration of AuNP is only a few percent by weight (TEM images also shows isolated individual Au NPs). Thus each individual AuNP can be treated as heat source generating local heating around the AuNP. The local increase in temperature around the individual nanoparticle depends on their absorption crosssection, intensity of the laser, well as conductivity of the surrounding medium. Finite-Difference Time-Domain (FDTD) method has been used to calculate the absorption crosssection of our Au/R-TiO_2 nanoparticles. The bulk dielectric function tabulated by Johnson and Christy has been used for gold[9], and a dielectric constant of 2.75 has been used for Rutile (R-TiO_2)[10]. Calculations have been performed for a longitudinal polarized excitation. Fig. S6a shows normalized absorption spectra for gold nanoparticle size ranging from 6 nm to 21 nm, which corresponds to the experimental size distribution. The modeled Au/R-TiO_2 nanoparticle is shown as inset. The calculated spectra exhibit two resonances: (i) a resonance located at ~515 nm corresponding to the dipolar LSPR of the AuNP semi-embedded in R-TiO_2 and partially exposed to the air, (ii) a resonance located between 615 nm and 640 nm associated to a cavity mode generated in the R-TiO_2 nanoparticle.

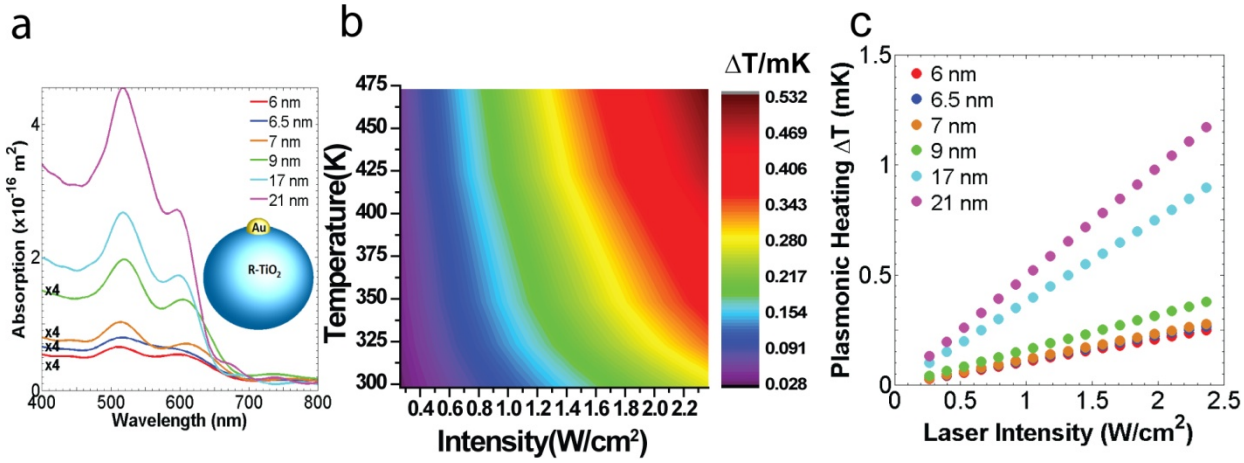

Figure S6 | a, Calculated absorption spectra of AuNP ranging from 6 nm to 21 nm in diameter semi-embedded in a 30 nm Rutile nanoparticle. The inset shows the modeled system used in the FDTD calculations. **b,** Photothermal rate enhancement factor as a function of operating temperature using three laser intensities. **e,** Modeling plasmonic heating showing increase in temperature on individual AuNP (6.5 nm diameter, 1.75 wt% AuNP sample) embedded in TiO_2 matrix as a function of laser intensities as well as operating temperatures. **c,** The increase in plasmonic heating on four individual AuNPs embedded in TiO_2 at room temperature 298 K with increasing diameter.

In order to determine the effect of the laser induced plasmonic heating of nanoparticles on the photoreaction, a plasmonic heating model allows us to calculate the temperature increase ΔT on the surface of individual AuNP embedded in a TiO_2 matrix, as a function of incident laser intensity I using the following equation[11-15]

$$\Delta T=\sigma_{abs} I/(4\pi R\beta\kappa_m), \qquad \text{(S1)}$$

where σ_{abs} is the integrated absorption cross section over the entire visible range of 450-1,000 nm, R is the radius of spherical AuNP, β is the thermal capacitance coefficient depending on the nanoparticle aspect ratio ($\beta=1+0.96587[\ln^2(AR)]$, $\beta=1$ for a spherical nanoparticle), and κ_m denotes the temperature dependent thermal conductivity[16, 17] of surrounding dielectric (R-TiO_2)

respectively. A contour plot with ΔT as a function of temperature and laser intensity shows only a ~0.5 mK maximum rise in overall nanoparticle surface temperature for a 6.5 nm diameter nanoparticle, even with 2.4 W/cm^2 laser power at 200^{o}C (Fig. S6b). Figure S6c shows the results of plasmonic heating for AuNP sizes ranging from 6 nm to 21 nm at 298 K. It can be seen that only a ~ 0.25mK or less maximum rise in overall nanoparticle (<9 nm) surface temperature even for an incident laser power of 2.4 W/cm^2. Larger AuNPs (17-21 nm) give rise to a maximum temperature increase below 1.25 mK at highest operating laser power. This supports our conclusion that photothermal heating is not causing the observed HD formation. The small increase in the local nanoparticle temperature on the nanoparticle surface is due to low laser intensities used as well as lower absorption crosssection of small AuNP as compared to bigger nanoparticles. Thus around 2-5 K increase in the catalyst temperature at high laser intensities is nothing but accumulative heating due to large number or nanoparticle in the overall photocatalyst. We also conclusively show that that increment of local heating cannot account for the observed photocatalytic rate in Fig. 2b.

S7. Local field enhancement

To further explore the possible effect of the local electric field on the photoreaction, we calculated the near-field enhancement at the LSPR for a 7 nm AuNP semi-embedded in a 30 nm R-TiO_2 nanoparticle.

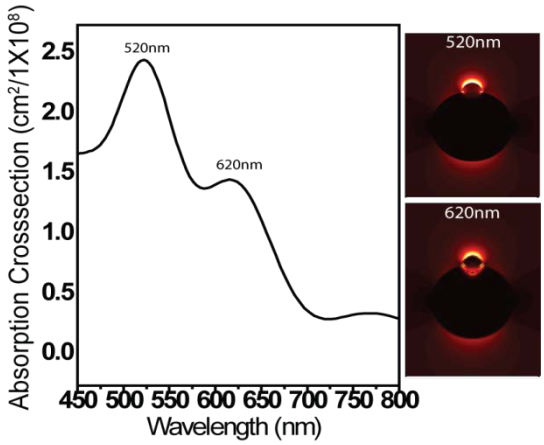

Figure S7 | FDTD calculated absorption crosssection of a 7 nm AuNP semi embedded in a 30 nm TiO_2 showing dipolar plasmon mode at 520 nm and a cavity plasmon mode at 620 nm. The corresponding near field enhancement plots are depicted beside.

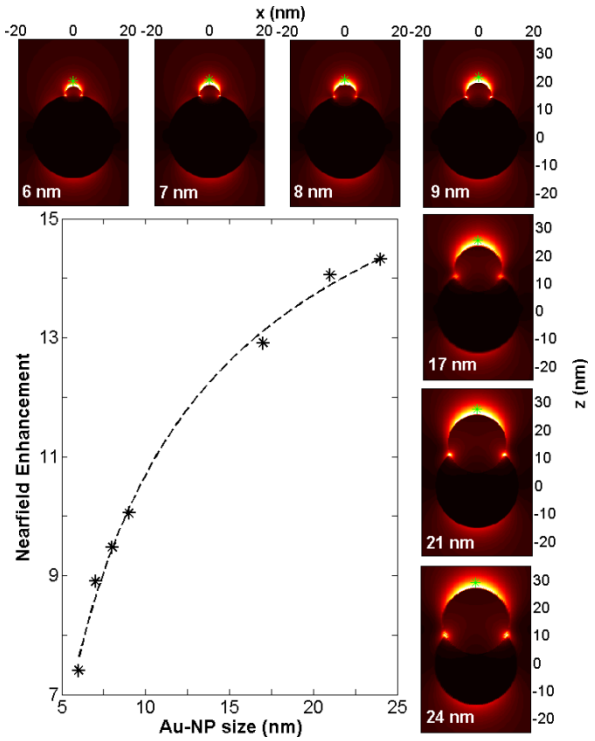

Figure S8 | Near field plots as a function of particle size Near-field enhancement associated to the dipolar LSPR plotted as a function of AuNP sizes. The values of the near-field are calculated 2 nm above the AuNP (green dots on the near-field maps). Clearly with increasing size of the AuNP the near field becomes more pronounced. In each case TiO_2 has a 30nm diameter.

The results show that the maximum field enhancement is located on top of the AuNP which is exposed to the air (Fig. S7 and S8). The size dependence of the near-field enhancement calculated at 2 nm above the AuNP (green dots on the near-field plots) clearly shows that the local electric field increases with the AuNP size. This size effect is contrary to the photoreaction tendency presented in our work, thus proving that the near-field cannot be responsible for the H_2 dissociation.

S8. First principles calculations

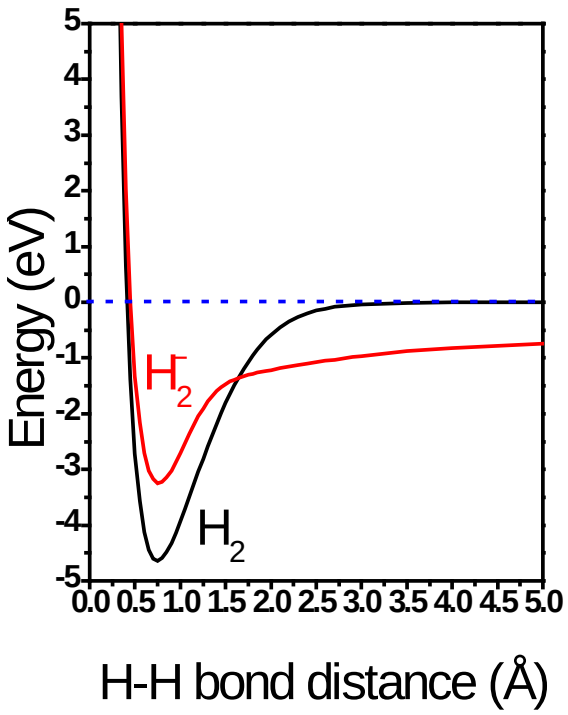

Figure S9 | Energy of the isolated neutral (H_2) and charged (H_2^-) hydrogen molecule as a function of bond length using CASSCF (2 electrons in 2 orbitals) and CASPT2 calculations. For the isolated molecules (i.e., without a Au surface) the dissociation energy for H_2 is substantially larger (-4.6 eV) than for H_2^- (2.6 eV).

The isolated H_2 molecule features a comparatively high dissociation energy of over 4 eV (see Fig. S9). Indeed, even isolated H_2^- decays by ejection of an electron rather than by dissociation (see Fig. S9). As shown in earlier work[18], H_2^- forms a metastable resonance (called a Feshbach resonance) 1.7 eV above the ground state of H_2, with comparatively long lifetime, that can decay (to H_2) by ejecting an electron. Upon contact with a metal surface, the resonant H_2^- state broadens substantially (put differently, the lifetime of the resonance decreases by interaction with the surface). Indeed, the antibonding $1\sigma^*$ of H_2 may become (depending on the Fermi level of the metal) partially occupied, corresponding to an admixture of the H_2^- state and metal surface states. This is especially true for Au (see Löwdin charge analysis in Fig. S10 and Fig. 2b of the main manuscript), making hydrogen adsorption on a clean Au (111) surface energetically unfavorable. For larger H-H separation, however, a dissociated, chemisorbed state emerges (see Fig. 6 of the main manuscript). Dissociation towards this state is suppressed by a substantial energy barrier at the intermediate transition state (marked in Fig. 2c). This barrier may substantially be reduced by inserting hot electrons from the surface into the antibonding σ^* orbital (see main manuscript).

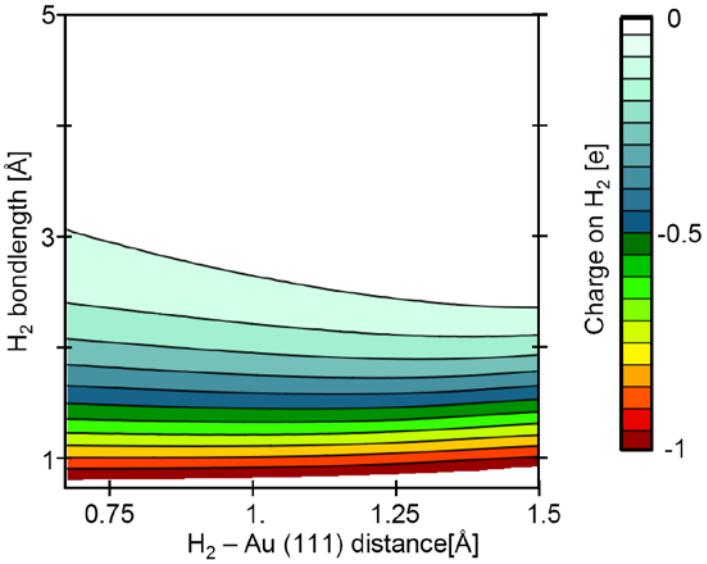

Figure S10 | Ground state embedded CI-Singles Löwdin charge on H_2 molecule as it approaches Au (111) as a function of H_2-Au surface separation and H-H bond length. Negative charge on H_2 increases as H_2 approaches the surface. Contour line separation is 0.05*e*.

To elucidate this hot electron transfer process, we performed density functional theory (DFT) and embedded correlated wavefunction calculations. The latter allows for a treatment of excited states, representing the hot electron. We do not explicitly include the TiO_2 substrate: its main effect is to slightly charge the gold cluster, further aiding the charge transfer process[23]. We choose the clean (111) facet as most stable surface. The experimental gold clusters are large enough to not require many edges for geometrical reasons. Additional defects or edge dislocations can further aid the dissociation process. Embedded CI-Singles as well as CASPT2 calculations both consistently show that the charge on H_2 slowly increases upon approaching the Au(111) surface (for ground state and excited states), corresponding to a gradual filling of the antibonding $1\sigma*$ orbital (Fig. S10 and Fig. 6b in the main manuscript). Below, we briefly summarize the technical details of our two methods.

Spin-polarized DFT calculations were performed using the VASP program[19], with the default projector-augmented-wave (PAW) Au and H potentials. We model a 3×3 Au (111) slab containing 7 atomic layers, separated by 20 Å of vacuum from its image imposed by the periodic boundary conditions. We include two H_2 molecules on the bottom and top of the slab to avoid dipole interactions. We use a 6x6x1 Monkhorst-Pack grid, 0.1 eV Fermi-Dirac smearing, 250 eV plane-wave cutoff and the PBE functional for exchange and correlation[20]. For the embedding, we follow the procedure outlined in our previous work[21]. To calculate the embedding potential, we consider a 5×5 supercell with 4 atomic layers, containing 100 atoms. We use a larger unit cell to

avoid artifacts of the periodic boundary conditions affecting the embedded cluster. We use the abinit[22, 23] program to obtain a reference density inside the periodic Au (111) slab (without the PAW formalism, to be consistent with the effective core potentials (ECPs) employed in the embedded cluster). Subsequently, we partition the slab into a 14-atom Au cluster and a surrounding environment. Finally, we determine a global, unique embedding potential V, so that independent solutions for cluster and environment together reproduce the reference density of the entire slab. Since we do not use PAW potentials, we need a plane-wave basis kinetic energy cutoff of 700 eV. Since the real-space unit cell is larger than before, the k-point sampling is reduced to 4×4×1.

For the cluster calculations, we employ an augmented pVTZ basis set for H[24] and an uncontracted Hay-Wadt (3s,3p,4d) basis set, including an 11-electron ECP for Au[25], to be consistent with the 11-electron norm-conserving pseudopotential provided by abinit. For contracted or smaller basis sets, we find substantial basis set superposition errors as the hydrogen molecule approaches. We validated our Au basis set choice by comparing ionization energies to all-electron calculations and find satisfactory agreement. We use the MOLCAS[26] and GAMESS[27] software packages, both modified to include the embedding potential. For an accurate description of the ground state, we perform a second-order multi-reference many-body perturbation theory correction (CASPT2) correction on top of a complete-active-space (CASSCF) calculation. Our active space consists of 6 electrons in 6 orbitals (the H_2 and the four $6s^1$ Au electrons closest to the adsorption site). To obtain a detailed picture of excited states, we perform both state-averaged CASSCF as well as Configuration-Interaction-Singles (CIS) calculations. State averaging has to be used as otherwise the orbital optimization of the CASSCF approach will not represent excited states adequately. Since the perturbative CASPT2 ansatz

nevertheless might not reproduce well excited states featuring different character than the ground state, we additionally perform CIS calculations, which have been shown to give qualitative insight into the excited states of clusters[28]. For both methods, we calculate 10 excited state PESs (see, e.g., Fig. 4d in main text), that produce, for both approaches, qualitatively very similar results: we consistently find a reduced energy barrier towards dissociation for the sixth excited state, at an energy of about 1.8 eV, close to the Feshbach resonance of H_2 (see Fig. S10). We include a basis-set-superposition error (BSSE) correction to correct for finite basis set errors when approaching the Au with the H_2.

S9. The isotope effect In the absence of any other competing diatomic molecule, the dissociation probability of H_2 and D_2 is 50%. However; the dissociation rate D_2 will be slower as compared to H_2. This is because D_2, being twice as heavy as H_2, will have a much slower rate of nuclear translational motion along its excited state potential energy surface[29]. Because of the resulting shorter internuclear distance, D_2 will retain more vibrational energy than H_2, resulting in a larger energy requirement for dissociation. However, once dissociated, atomic H and D can combine with each other to produce HD, which subsequently desorbs from the Au NP surface. The surface diffusion rate of atomic D should be less than that of atomic H, since diffusion coefficients vary inversely with the mass of the gas molecule. Thus recombination of atomic H to produce H_2 will proceed on the Au NP surface at a faster rate than the production of HD and D_2.

S10. Stability of photocatalyst and effect of spillover

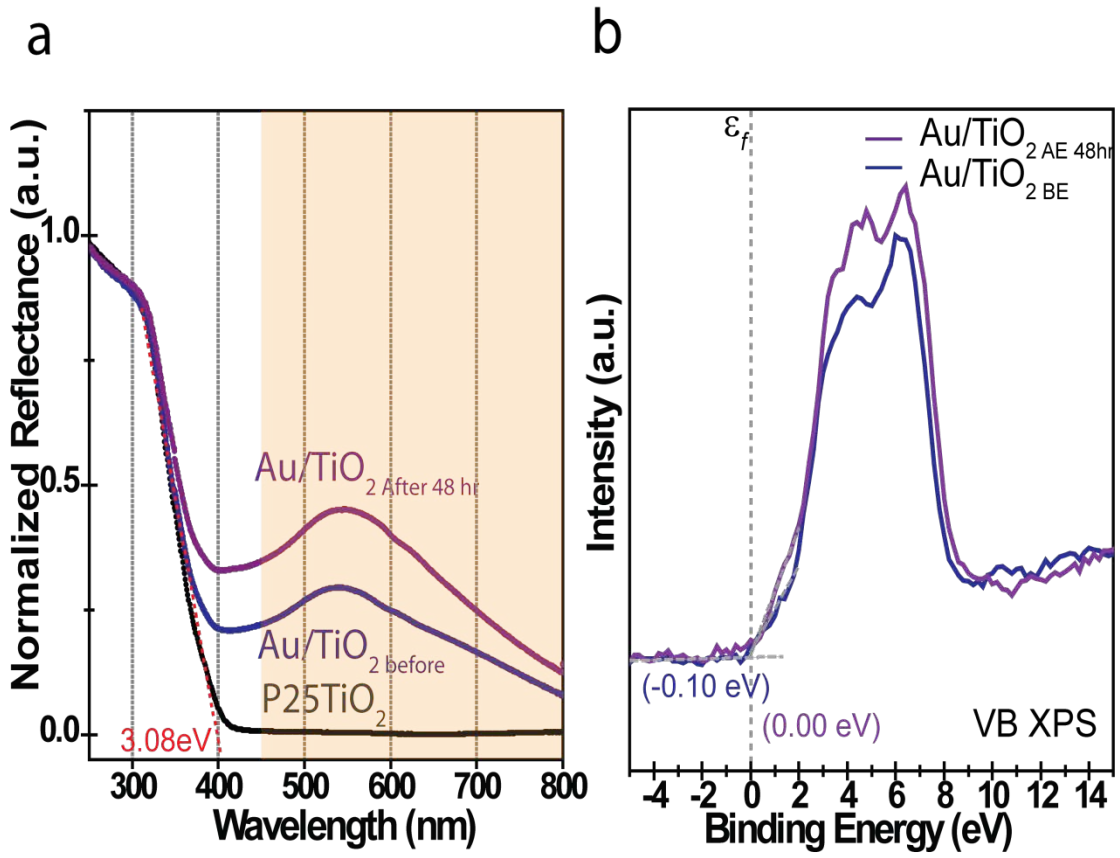

Figure S11 | a, Uv-Vis diffuse reflectance spectrum of pristine P25-TiO_2 (black), 1.75 wt% Au/TiO_2 before experiment (blue) and after 2 days of experiment (violet). Yellow shaded area showing the visible wavelength range. **b,** VB XPS measurement of 1.75 wt% Au/TiO_2 before experiment (blue) and after 2 days of experiments (violet) showing negligible shift in VB signifying negligible shift of band edge.

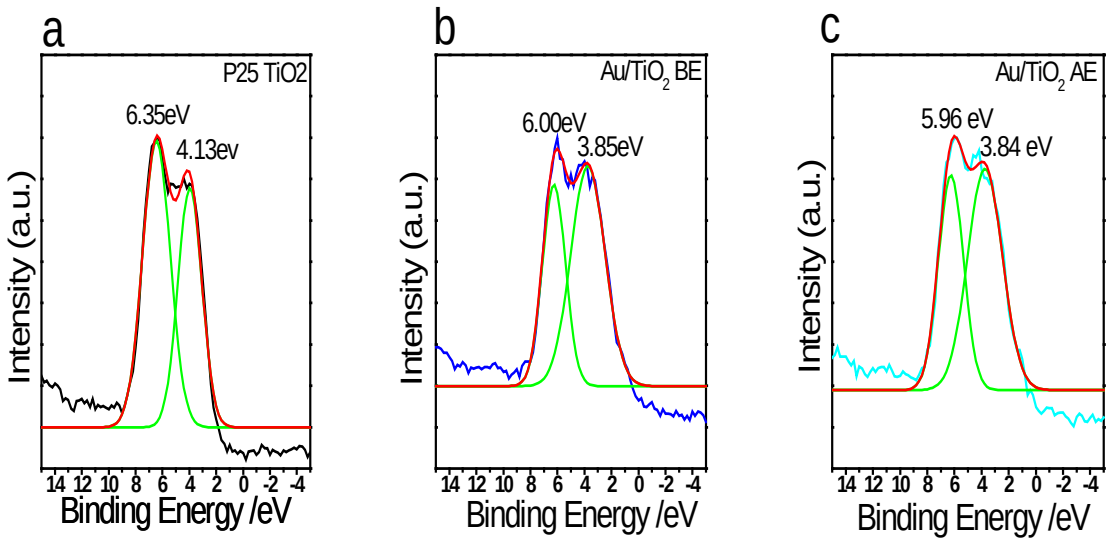

Figure S12 |VB XPS data Gaussian Fits for VB XPS of **a,** pristine P25 TiO_2 **b,** Au/TiO_2 before experiment and **c,** Au/TiO_2 after experiment.

To show the stability of the photocatalyst, UV-Vis spectra of TiO_2 and the photocatalyst sample (1.75 wt%) before and after 48 hours under experimental conditions, is shown in Fig. 5b. No dramatic changes in the plasmon resonance were observed, except for changes in the relative amplitudes of the plasmon peak, which probably is due to sintering of the sample and particle agglomeration at high temperatures[29]. From the reflectance spectrum of pristine TiO_2 shown in Fig. 5b we also establish that within the wavelength range of our photoreactivity experiments (shown as shaded areas in Fig.S11a) all incident illumination was below the band gap of TiO_2 (3.08 eV).

One of the common effects of dissociating H_2 on Au/TiO_2photocatalysts is diffusion of H atoms into the TiO_2[30-32]. After the initial dissociation on the surface, atomic H or D can freely diffuse and become incorporated in the TiO_2 as localized Ti-O(H)-Ti species. This creates shallow defect trap states lying below the conduction band which may lead to TiO_2 absorption at visible

wavelengths, increasing photocatalytic activity in the visible part of spectrum. To determine whether any significant incorporation of H or D into TiO_2 occurred over the course of our experiments, the density of states of a representative Au/TiO_2 sample was measured using Valence Band X-ray Photoelectron Spectroscopy (performed on 1.75 wt% Au/TiO_2 photocatalyst before and 48 hours after the experiment; Fig. S11b). This measurement show negligible changes over the wavelength range of the present experiments (450-800 nm) and thus rules out the effect of trap states on the photodissociation process. Also, there is no relative shift in binding energy peaks before and after photocatalyst use (Fig. S12 b and c).

There might be active sites on TiO_2 for dissociative adsorption of H_2 as well. The surface defect sites causing oxygen vacancies have been found to act as electron donor sites, forming a Titanium hydride Ti^{4+}-H^- bond. This may contribute to autodissociation or thermal dissociation of H_2, but since we are not exciting the TiO_2 bandgap this may not contribute to photodissociation. Another important factor behind the auto- or thermal dissociation of H_2 may be the slightly anionic nature of Au over reducible oxides like TiO_2, due to the possible charge transfer from the TiO_2 matrix into Au[33,34]. Experiments performed in ultrahigh vacuum using Fourier Transform Spectroscopic measurements can confirm the existence of active site in TiO_2 in photochemical processes[35]. However, the objective of our present study was to investigate whether Au nanoparticle plasmon-induced hot electrons could provide a mechanism for the direct, visible wavelength photodissociation of H_2.

References

1. Hugon, A.; Delannoy, L.; Louis, C. ***Gold Bull.*** **2008, 41, (2), 127-138.**
2. Zanella, R.; Giorgio, S.; Henry, C. R.; Louis, C. ***J.Phys. Chem. B*** **2002, 106, (31), 7634-7642.**
3. Haruta, M. ***Catal. Today***
1997, 36, (1), 153-166.
4. MurdochM; Waterhouse, G. I. N.; Nadeem, M. A.; Metson, J. B.; Keane, M. A.; Howe, R. F.; LlorcaJ; IdrissH. ***Nat Chem*** **2011, 3, (6), 489-492.**
5. Tsukamoto, D.; Shiraishi, Y.; Sugano, Y.; Ichikawa, S.; Tanaka, S.; Hirai, T. ***Journal of the American Chemical Society*** **2012, 134, (14), 6309-6315.**
6. Zwijnenburg, A.; Goossens, A.; Sloof, W. G.; Crajé, M. W. J.; van der Kraan, A. M.; Jos de Jongh, L.; Makkee, M.; Moulijn, J. A. ***J. Phys. Chem. B*** **2002, 106, (38), 9853-9862.**
7. Kreibig U.; Vollmer M., ***Optical Properties of Metal Clusters*****. 1995; Vol. 25.**
8. Scholl, J. A.; Koh, A. L.; Dionne, J. A. ***Nature*** **2012, 483, (7390), 421-427.**
9. Johnson, P. B.; Christy, R. W. ***Phys. Rev. B: Condens. Matter*** **1972, 6, (12), 4370-4379.**
10. Fisher, J.; Egerton, T. A., Titanium Compounds, Inorganic. In ***Kirk-Othmer Encycl. Chem. Technol.,*** **John Wiley & Sons, Inc.: 2000.**
11. Baffou, G.; Quidant, R.; García de Abajo, F. J. ***ACS Nano*** **2010, 4, (2), 709-716.**
12. Baffou, G.; Quidant, R.; Girard, C. ***Appl. Phys. Lett.*** **2009, 94, (15), 153109-3.**
13. Govorov, A.; Zhang, W.; Skeini, T.; Richardson, H.; Lee, J.; Kotov, N. ***Nanoscale Res. Lett.*** **2006, 1, (1), 84 - 90.**
14. Govorov, A. O.; Richardson, H. H. ***Nano Today*** **2007, 2, (1), 30-38.**
15. Huschka, R.; Zuloaga, J.; Knight, M. W.; Brown, L. V.; Nordlander, P.; Halas, N. J. ***J Am Chem Soc*** **2011, 133, (31), 12247-12255.**
16. Thurber, W. R.; Mante, A. J. H. ***Phys. Rev.*** **1965, 139, (5A), A1655-A1665.**
17. Yoshida, I. ***J. Phys. Soc. Jpn.*** **1960, 15.**
18. McWeeny, R. ***J. Mol. Struct. THEOCHEM*** **1992, 261, (0), 403-413.**
19. Kresse, G.; Furthmüller, J. ***Comp. Mater. Sci.*** **1996, 6, (1), 15-50.**
20. Perdew, J. P.; Burke, K.; Ernzerhof, M. ***Phys. Rev. Lett.*** **1996, 77, (18), 3865-3868.**
21. Libisch, F.; Huang, C.; Liao, P.; Pavone, M.; Carter, E. A. ***Phys. Rev. Lett.*** **2012, 109, 198303.22. Gonze, X.; Amadon, B.; Anglade, P. M.; Beuken, J. M.; Bottin, F.; Boulanger, P.; Bruneval, F.; Caliste, D.; Caracas, R.; Côté, M.; Deutsch, T.; Genovese, L.; Ghosez, P.; Giantomassi, M.; Goedecker, S.; Hamann, D. R.; Hermet, P.; Jollet, F.; Jomard, G.; Leroux, S.; Mancini, M.; Mazevet, S.; Oliveira, M. J. T.; Onida, G.; Pouillon, Y.; Rangel, T.; Rignanese, G. M.; Sangalli, D.; Shaltaf, R.; Torrent, M.; Verstraete, M. J.; Zerah, G.; Zwanziger, J. W.** ***Comput. Phys. Commun.*** **2009, 180, (12), 2582-2615.**
23. Gonze, X. ***Zeit. Kristallogr.*** **2005, 220, 558-562.**
24. Dunning, J. T. H. ***J. Chem. Phys.*** **1989, 90, (2), 1007-1023.**
25. Hay, P. J.; Wadt, W. R. ***J. Chem. Phys.*** **1985, 82, (1), 270-283.**
26. Aquilante, F.; De Vico, L.; Ferré, N.; Ghigo, G.; Malmqvist, P.-å.; Neogrády, P.; Pedersen, T. B.; Pitoňák, M.; Reiher, M.; Roos, B. O.; Serrano-Andrés, L.; Urban, M.; Veryazov, V.; Lindh, R. ***J. Comput. Chem.*** **2010, 31, (1), 224-247.**
27. Schmidt, M. W.; Baldridge, K. K.; Boatz, J. A.; Elbert, S. T.; Gordon, M. S.; Jensen, J. H.; Koseki, S.; Matsunaga, N.; Nguyen, K. A.; Su, S.; Windus, T. L.; Dupuis, M.; Montgomery, J. A. ***J. Comput. Chem.*** **1993, 14, (11), 1347-1363.**

28. Closser, K. D.; Head-Gordon, M. *J. Phys. Chem. A* 2010, 114, (31), 8023-8032.
29. Christopher, P.; Xin, H.; Linic, S. *Nat Chem* 2011, 3, (6), 467-472.
30. Panayotov, D. A.; Burrows, S. P.; Yates, J. T.; Morris, J. R. *J. Phys. Chem. C* 2011, 115, (45), 22400-22408.
31. Panayotov, D. A.; Yates, J. T. *J. Phys. Chem. C* 2007, 111, (7), 2959-2964.
32. Conner, W. C.; Falconer, J. L. *Chem. Rev.* 1995, 95, (3), 759-788.
33. Laursen, S.; Linic, S. *Phys. Rev.Lett.* 2006, 97, (2), 026101.
34. Zhang, Z.; Yates, J. T. *Chem. Rev.* 2012.
35. Green, I. X.; Tang, W.; Neurock, M.; Yates, J. T. *Science* 2011, 333, (6043), 736-739.